

# Land Surface Temperature Retrieval From Channel Resolution Enhanced FY-3D/MWRI Observations

Binqian Wang, Fang-Cheng Zhou, Pei Leng<sup>ID</sup>, Senior Member, IEEE, Yihong Bai, Xia Zhang, and Guo-Fei Shang

**Abstract**— Land surface temperature (LST) is a critical parameter in meteorology, hydrology, and environmental science. Compared to thermal infrared (TIR) remote sensing, passive microwave (PMW) remote sensing for LST retrieval offers advantage under cloudy conditions. In this study, we utilized the channel resolution enhanced (CRE) microwave radiation imager (MWRI) brightness temperature data from Chinese FengYun-3D (FY-3D) polar-orbiting meteorological satellite as the primary input to obtain global LST. Two physics-based PMW retrieval methods were introduced: the three-channel method (18.7, 36.5, and 89.0 GHz) and the precipitable water vapor (PWV)-cloud liquid water (CLW) method, which integrates the 18.7- and 23.8-GHz channels with PWV and CLW. The results indicate that both methods have generally achieved good accuracy. The three-channel method performs well in grasslands and barren lands during the daytime, with a root-mean-square error (RMSE) ranging from 4 to 5 K. At night, it excels in grasslands, croplands, and barren lands, with an RMSE from 2 to 3 K. The PWV-CLW method demonstrates superior accuracy for forests and croplands during the daytime, with RMSE values from 3.6 to 5.3 K. At night, this method excels in accuracy for forests, with an RMSE of 2.9 K. Additionally, a fusion method was proposed to improve the overall accuracy of LST estimation across different land cover (LC) types. The RMSE values for ascending and descending overpasses are 4.22 and 2.76 K, with biases of -0.29 and -0.6 K, respectively. This approach effectively mitigates spatial heterogeneity and atmospheric effects, enabling all-weather LST retrieval and showcasing the potential of CRE FY-3D/MWRI data for LST monitoring.

**Index Terms**— Channel resolution enhanced (CRE) FengYun-3D (FY-3D)/microwave radiation imager (MWRI), land surface temperature (LST), passive microwave (PMW), precipitable water vapor (PWV)-cloud liquid water (CLW) method, thermal infrared (TIR), three-channel method.

Received 23 January 2025; revised 31 March 2025; accepted 17 April 2025. Date of publication 21 April 2025; date of current version 1 May 2025. This work was supported in part by the National Natural Science Foundation of China under Grant 42271384 and in part by the Joint Funds of the National Natural Science Foundation of China under Grant U2242211. (Binqian Wang and Fang-Cheng Zhou contributed equally to this work.) (Corresponding author: Pei Leng.)

Binqian Wang is with the State Key Laboratory of Efficient Utilization of Arable Land in China, Institute of Agricultural Resources and Regional Planning, Chinese Academy of Agricultural Sciences, Beijing 100081, China, and also with the School of Land Resources and Urban-Rural Planning, Hebei GEO University, Shijiazhuang 050030, China (e-mail: 15330318196@163.com).

Fang-Cheng Zhou and Yihong Bai are with the National Satellite Meteorological Center, Beijing 100082, China (e-mail: zhoufc@cma.gov.cn; baiyh@cma.gov.cn).

Pei Leng is with the State Key Laboratory of Efficient Utilization of Arable Land in China, Institute of Agricultural Resources and Regional Planning, Chinese Academy of Agricultural Sciences, Beijing 100081, China (e-mail: lengpei@caas.cn).

Xia Zhang and Guo-Fei Shang are with the School of Land Resources and Urban-Rural Planning, Hebei GEO University, Shijiazhuang 050030, China (e-mail: zhangxia396@hgu.edu.cn; shangguofei@hgu.edu.cn).

Digital Object Identifier 10.1109/TGRS.2025.3562859

## I. INTRODUCTION

LAND surface temperature (LST) is a key physical variable that reflects the interaction between the Earth's surface and the atmosphere [1], [2], [3], and it plays a critical role in studies related to climate change, agricultural production, environmental monitoring, and ecosystem responses [4], [5], [6]. Due to rapid changes in surface properties, LST exhibits significant spatial heterogeneity and temporal variability, making it difficult for traditional ground-based measurements to provide comprehensive spatial coverage. Satellite remote sensing offers an effective and feasible method for acquiring global, high-precision LST data.

Currently, satellite thermal infrared (TIR) remote sensing is widely employed in various algorithms for LST retrieval [7], [8]. These algorithms include single-channel [9], [10], multichannel [11], split-window [12], [13], [14], and temperature-emissivity separation methods [15], [16]. LST values derived from TIR measurements generally offer high spatial resolution and accuracy. The high precision of TIR-based LST retrieval methods, combined with the availability of TIR LST products, makes TIR remote sensing the primary data source for LST-related research. However, the advantages of TIR remote sensing are limited to cloud-free conditions, as clouds are nearly opaque to TIR radiation. Actually, approximately 60% of the Earth's land surface is often covered by clouds. This limitation restricts the broader application of TIR remote sensing in regions with frequent cloud cover [17], [18].

Compared with the shorter wavelengths of TIR, the longer wavelengths of passive microwave (PMW) signals emitted from the Earth's surface allow cloud penetration and detection by spaceborne remote sensors, facilitating the retrieval of LST under clouds. Therefore, PMW has emerged as a primary approach for retrieving all-weather LST [19]. However, a critical limitation of PMW lies in its coarse spatial resolution, which restricts its application for high-detail land surface analysis. The methods for LST retrieval based on PMW can be broadly classified into empirical, semiempirical, physical-statistical, and machine learning approaches. Empirical and semiempirical methods are typically based on regression models that relate microwave brightness temperature to LST [20], [21], [22], [23], [24], [25]. McFarland et al. [20] were among the first to develop empirical equations for retrieving LST from special sensor microwave imager (SSM/I) data for farmlands, dry soils, and wet soils. Over time, additional environmental variables were introduced to improve the accuracy of LST retrieval, thus enhancing the precision and applicability of

these models in various environmental conditions. Although these methods are relatively simple and convenient, requiring only satellite-derived brightness temperature data as input, their applications are often constrained by the region of interest. Machine learning methods, by contrast, do not require the derivation of specific calculation rules for particular problems; instead, they rely on representative training datasets for learning and training. These methods can solve nonlinear problems in parallel without being limited by the equations themselves, effectively addressing ill-posed retrieval problems [26], [27], [28], [29], [30], [31]. However, these methods lack a clear physical foundation, and their accuracy heavily depends on the representativeness and completeness of the training dataset.

Physical models, on the other hand, are based on radiative transfer theory and offer clear physical interpretations, which make them particularly advantageous for long-term and large-scale LST retrieval. Since the 1990s, several physical methods have been developed to estimate LST. Basist et al. [32] proposed a three-channel retrieval method based on the theoretical relationship between microwave emissivity at different soil moisture levels, aiming to retrieve LST. Han et al. [33] improved this three-channel emissivity method by representing the emissivity adjustment term as a combination of different channel emissivities. Weng and Grody [34] introduced a physically based LST estimation method assuming that surface emissivities at two adjacent frequencies are approximately the same. They noted that the differences in brightness temperature measurements between two adjacent frequencies are mainly due to the varying absorption effects of precipitable water vapor (PWV). To improve LST retrieval, they incorporated a linear function of water vapor content (WVC) into a two-channel physical model. Huang et al. [35] further refined this approach by identifying a significant linear relationship between surface emissivity at 18.7 and 23.8 GHz. They introduced an additional regression coefficient to improve the performance of the two-channel physical model. In 2023, Huang et al. [36] made further advancements by considering the influence of clouds on microwave radiation. They introduced PWV and cloud liquid water (CLW) as input parameters for atmospheric correction, which significantly enhanced retrieval precision.

In the progression of PMW remote sensing retrieval research, several PMW sensors have been commonly used for LST retrieval. These include the Scanning Multichannel Microwave Radiometer (SMMR) onboard the Nimbus 7 satellite [37], the SSM/I on the Defense Meteorological Satellite Program (DMSP) satellite [38], the Advanced Microwave Scanning Radiometer for EOS (AMSR-E) aboard the Aqua satellite [39], and the Advanced Microwave Scanning Radiometer 2 (AMSR2) onboard the Global Change Observation Mission first Water (GCOM-W1) "SHIZUKU" satellite [40]. As part of Chinese meteorological satellite program, algorithms for LST retrieval from both geostationary and polar-orbit FengYun satellite data have been proposed in recent years [41], [42], [43]. For domestic FengYun satellites, the PMW LST retrieval algorithms using microwave radiation imager (MWRI) brightness temperature data have also demonstrated good applicability. Zhu et al. [44] applied

a statistical regression model to retrieve LST across various land cover (LC) types and complex environmental conditions. Wang et al. [45] developed a physically based retrieval method known as the University of Montana (UTM) land surface retrieval algorithm, which captured the spatial distribution and temporal trends of LST across China using FengYun-3D (FY-3D)/MWRI brightness temperature. Despite some studies, the overall body of research remains limited, and issues with large errors persist, particularly due to the relatively coarse spatial resolution of the data. However, MWRI brightness temperature products hold significant potential, highlighting the need for further investigation into high spatial resolution PMW LST retrieval algorithms to better leverage this sensor's capabilities.

The primary objective of this study is to assess the feasibility of employing two physical methods using channel resolution enhanced (CRE) FY-3D/MWRI data with a spatial resolution of 6.25 km to retrieve LST and to develop a fusion approach tailored to different LC types. The first method is a three-channel inversion technique based on the relationships between multichannel emissivity, while the second method, the PWV-CLW inversion approach, incorporates the effects of clouds on microwave radiation. By systematically evaluating the performance of both methods across various LC types, the study identifies the optimal method for each type and integrates them into an improved fusion framework. In this article, MODIS LST products, representing TIR skin temperature, are used as the true LST. The LST derived using the formula obtained through this calibration represents the surface's uppermost layer temperature, eliminating the need to convert subsurface temperature to skin temperature during validation. The organization of this article is as follows. Section II describes the remote sensing data used in this study. Section III outlines the development of the two research methods and provides the overall framework of the study. Section IV presents the results of PMW LST retrievals on a global scale with both methods. Section V discusses the results as applied to various LC types and compares the retrieval results of both methods. Building on these findings, a fusion approach is introduced, which selects the method with higher accuracy for fusion to achieve better overall performance. Finally, Section VI presents the conclusions.

## II. DATA

### A. CRE FY-3D MWRI Data

FY-3D is the fourth satellite in China's second-generation polar-orbiting meteorological satellite series. Launched in November 2017, it serves as the primary satellite for afternoon observations in low Earth orbit. MWRI is one of the key payloads aboard FY-3D. MWRI provides Earth observation capabilities across frequencies of 10.65, 18.7, 23.8, 36.5, and 89 GHz, with each frequency offering two polarization modes: vertical (*V*) and horizontal (*H*). The original spatial resolution of MWRI varies by frequency, ranging from 9 to 85 km, depending on the frequency. Detailed specifications are provided in Table I. The managing department of MWRI data, China Meteorological Administration (CMA), resamples the

TABLE I  
DETAILED CHARACTERISTICS OF THE FY-3D/MWRI

Frequency (GHz)	Bandwidth (MHz)	Polarization	Sensitivity (K)	Range (K)	Original spatial resolution (km × km)
10.65	180 ± 10 %		0.5		51 × 85
18.7	200 ± 10 %		0.5		30 × 50
23.8	400 ± 10 %	V, H	0.5	3 - 340	27 × 45
36.5	900 ± 10 %		0.5		18 × 30
89	2300 × 2 ± 10 %		0.8		9 × 15

original brightness temperature into 25-km spatial resolution to generate Level 1 products and releases them on its official website (<http://data.nsmc.org.cn/>).

The FY-3D/MWRI brightness temperature data used in this study are a CRE product. This product is generated through a super-resolution process that utilizes the scatterometer image reconstruction (SIR) algorithm to enhance the spatial resolution of the FY-3D/MWRI L1 data. The SIR algorithm improves spatial resolution based on redundant information resulting from the overlapped area of sensor footprints. Generally, the larger the overlapped area, the better the resolution enhancement. The SIR algorithm predicts the brightness temperature of a pixel based on maximum entropy estimation, followed by an iterative process that generates the final brightness temperature. Currently, the SIR algorithm has been used successfully in relation to the Soil Moisture Active Passive (SMAP) Radiometer, AMSR-E, SMMR, SSM/I, SSMIS, and FY-3D/MWRI [46]. The product provides CRE FY-3D/MWRI brightness temperature data with a spatial resolution of 6.25 km. In this study, the CRE brightness temperature data are spatially matched with MYD11C1, whose spatial resolution is 0.05°, with a nearest neighbor interpolation method.

#### B. PWV and CLW Data

PWV and CLW are critical input parameters in the PWV-CLW method. In the present study, PWV and CLW are obtained from the ERA5 reanalysis dataset (<https://cds.climate.copernicus.eu/>). ERA5 is the fifth generation of European Center for Medium-Range Weather Forecast's (ECMWF) atmospheric reanalysis, spanning from January 1950 to the present. It is produced by the Copernicus Climate Change Service (C3S) at ECMWFs. ERA5 provides a comprehensive global climate reanalysis dataset, widely used in climate research, weather forecasting, environmental monitoring, and various other fields. In this study, we used the total column PWV and total column CLW data. The ERA5 dataset has a spatial resolution of 0.25° × 0.25° (longitude × latitude) and a temporal resolution of 1 h. To ensure spatiotemporal consistency between FY-3D/MWRI observations and ERA5 reanalysis data, comprehensive matching procedures were implemented. Temporally, ERA5 variables with hourly temporal resolution were linearly interpolated to correspond to the FY-3D/MWRI observation times. Spatially, ERA5 datasets were resampled to 0.05° using a cubic convolution resampling method.

#### C. MODIS Products

The MODIS products used in this study include the daily LST/Emissivity product (MYD11C1) and the annual LC product (MCD12C1). Both the daily LST and annual LC products have a spatial resolution of 0.05°. The MODIS daily LST product belongs to Collection 6.1 and is a Level-3 global product. To ensure the highest data quality, only pixels with MODIS quality control values of 0 (good quality) are retained. The MODIS LC classification product MCD12C1 is used to determine the surface type of FY-3D pixels. The MCD12C1 product is a Level-3 product, integrating one year of observational data from the MODIS sensors on the Terra and Aqua satellites. The distribution of LC types is shown in Fig. 1. Furthermore, the Global 30 Arc-Second Elevation (GTOPO30) digital elevation model (DEM) is used to correct for the altitude effect on each pixel.

### III. METHODOLOGY

#### A. Three-Channel Retrieval Method

The three-channel method establishes relationships between emissivity at three different frequencies, enabling the retrieval of LST through radiative transfer models. Basist et al. [32] introduced a three-channel emissivity method, showing that land surface emissivity varies with frequency and surface humidity. As surface humidity decreases, emissivity increases, and the difference in emissivity between low and high frequencies diminishes. Based on the three-channel emissivity method, Han et al. [33] proposed an emissivity correction term at 18.7 GHz to improve the retrieval accuracy

$$\varepsilon_{0,18.7v} - \varepsilon_{18.7v} = (\varepsilon_{0,89v} - \varepsilon_{89v}) + (\varepsilon_{36.v} - \varepsilon_{18.7v}) + (\varepsilon_{89v} - \varepsilon_{36.5v}) + (\varepsilon_{0,18.7v} - \varepsilon_{89v}) \quad (1)$$

where  $\varepsilon_{0,18.7v}$  and  $\varepsilon_{0,89v}$  are the nominal emissivity over dry ground at 18.7 and 89 GHz, respectively; and  $\varepsilon_{18.7v}$ ,  $\varepsilon_{36.5v}$ , and  $\varepsilon_{89v}$  are surface emissivity at 18.7, 36.5, and 89 GHz, respectively.

Based on simulation analysis by Han et al. [33], the first item on the right-hand side of (1) can be quantified as a quadratic function of the difference between emissivities at 36.5 and 89 GHz. Moreover, the last item on the right-hand side can be quantified as a constant. Consequently, the land surface emissivity at 18.7 GHz can be represented as

$$\varepsilon_{18.7v} = \varepsilon_{0,18.7v} - (\varepsilon_{36.5v} - \varepsilon_{18.7v}) - \alpha(\varepsilon_{89v} - \varepsilon_{36.5v}) - \beta(\varepsilon_{89v} - \varepsilon_{36.5v})^2 - \gamma \quad (2)$$

where  $\alpha$ ,  $\beta$ , and  $\gamma$  are the regression coefficients.

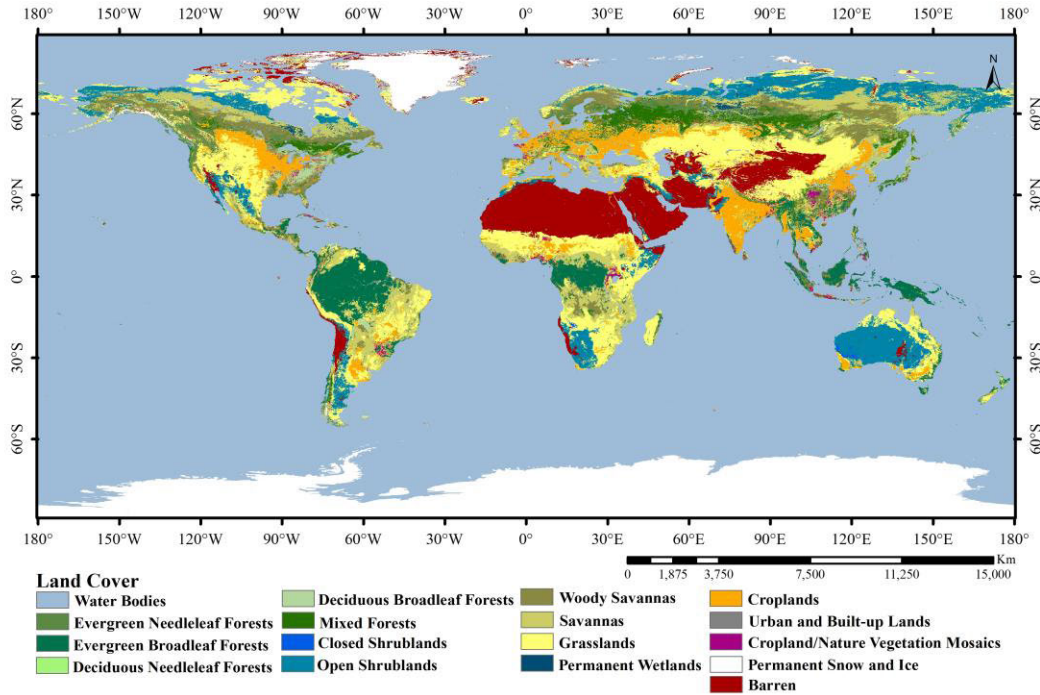


Fig. 1. Global LC map in 2022 before recategorization.

Neglecting the atmospheric effects of microwave radiation, the estimation of microwave brightness temperature can be expressed as

$$T_b(v) = \varepsilon_s(v)T_s \quad (3)$$

where  $T_b(v)$  is the brightness temperature at frequency  $v$  and  $T_s$  is the LST.

By combining (2) and (3), the LST can ultimately be expressed as

$$T_1 = T_{b18.7v} \quad (4)$$

$$T_2 = T_{b36.5v} - T_{b18.7v} \quad (5)$$

$$T_3 = T_{b89v} - T_{b36.5v} \quad (6)$$

$$T_s = \frac{T_1 + T_2 + \alpha T_3 + \beta T_3^2}{\varepsilon_{0,18.7v} - \gamma} \quad (7)$$

where  $T_{b18.7v}$ ,  $T_{b36.5v}$ , and  $T_{b89v}$  are the vertically polarized brightness temperatures at 18.7, 36.5, and 89 GHz, which are obtained from satellite brightness temperatures.

As noted, accurately determining the emissivity of dry surfaces is challenging due to its dependence on soil texture and type. Additionally, the variation in the denominator item on the right-hand side of (7) is small [33]. Consequently, in the development of the formula, simulated mean values are used to approximate the emissivity of dry surfaces. The LST can ultimately be expressed as

$$T_s = AT_1 + BT_2 + CT_3 + DT_3^2 + E \quad (8)$$

where  $A$ ,  $B$ ,  $C$ ,  $D$ , and  $E$  are coefficients.

#### B. PWV-CLW Method

The dual-channel physical method integrates the relationship between the emissivity/transmissivity of adjacent

channels into the radiative transfer model. The radiative transfer equation considering atmospheric effects can be expressed as

$$T_b = \varepsilon\tau T_s + (1 - \varepsilon)T_{ad}\tau + T_{au} \quad (9)$$

where  $T_b$  is the brightness temperature,  $\varepsilon\tau T_s$  is the first part,  $\varepsilon$  is the land surface emissivity,  $\tau$  is the atmospheric transmittance, and  $T_s$  is LST.  $(1 - \varepsilon)T_{ad}\tau$  is the second part,  $T_{ad}$  is the atmospheric downward radiation and cosmic background radiation is neglected, and  $T_{au}$  is the atmospheric upward radiation as the third part.

$T_{ad}$  and  $T_{au}$  can be approximated by (10) for PMW sensor with an Earth incidence angle at  $53^\circ$  as follows:

$$T_{ad} = T_{au} = (1 - \tau)T_m \quad (10)$$

where  $T_m$  is the atmospheric effective temperature.

Substituting (10) into (9) can yield [35]

$$T_b = [1 - (1 - \varepsilon)\tau^2]T_s - [1 + (1 - \varepsilon)\tau](1 - \tau)(T_s - T_m). \quad (11)$$

Combining the brightness temperatures at 18.7- and 23.8-GHz vertically polarized channels, the term  $[1 + (1 - \varepsilon)\tau](1 - \tau)(T_s - T_m)$  is relatively complicated and related to four different variables. Its value is located in the range between  $-2$  and  $10$  K in the simulated database and has a noticeable linear relationship with PWV. Therefore, it can be rewritten as a linear function of PWV.

Combining the brightness temperatures at 18.7- and 23.8-GHz vertically polarized channels, the following relationship can be deduced from (11):

$$\frac{T_s - T_{b18.7v} - a_1 \text{PWV}}{T_s - T_{b23.8v} - a_2 \text{PWV}} = \frac{(1 - \varepsilon_{18.7v})\tau_{18.7}^2}{(1 - \varepsilon_{23.8v})\tau_{23.8}^2} \quad (12)$$

TABLE II  
CORRESPONDING MODIS LC DATA CLASSIFICATION CODES AND THOSE AFTER RECATEGORIZATION

Code and type of MCD12C1	Code and definition after re-categorization
1 - Evergreen Needleleaf Forests	
2 - Evergreen Broadleaf Forests	
3 - Deciduous Needleleaf Forests	1 - Forests
4 - Deciduous Broadleaf Forests	
5 - Mixed Forests	
6 - Closed Shrublands	
7 - Open Shrublands	
10 - Grasslands	2 - Grasslands
8 - Woody Savannas	
9 - Savannas	
12 - Croplands	3 - Croplands
14 - Cropland/Nature Vegetation Mosaics	
16 - Barren	4 - Barren
0 - Water Bodies	
11 - Permanent Wetlands	
13 - Urban and Built-up Lands	-
15 - Permanent Snow and Ice	
255 - Unclassified	

where  $T_{b18.7v}$  and  $T_{b23.8v}$  are the vertically polarized channel brightness temperatures at 18.7 and 23.8 GHz, respectively; and  $a_1$  and  $a_2$  are coefficients. In [35], the simulations revealed a clear linear relationship between surface emissivity at the 18.7- and 23.8-GHz vertical polarization channels. Additionally, atmospheric transmittance in both channels is predominantly influenced by PWV and CLW. Consequently, the ratio of atmospheric transmittance between the two channels can be expressed as an exponential function of PWV and CLW. By further manipulating the formula, the final form of the LST retrieval method is derived

$$T_s = \frac{a_1 e^{a_2 \text{PWV} + a_3 \text{CLW}} (T_{b23.8v} + a_4 \text{PWV}) - (T_{b18.7v} + a_5 \text{PWV})}{a_1 e^{a_2 \text{PWV} + a_3 \text{CLW}} - 1} \quad (13)$$

where  $a_1-a_5$  are coefficients.

### C. Recategorization of MODIS LC Types

In this study, MODIS LC data are matched with corresponding FY-3D brightness temperature data. When evaluating the suitability of the model for different land classes, cloud contamination of MODIS LST products results in insufficient training samples for some land classes, particularly in areas with high vegetation, which are often excluded due to poor pixel quality. Furthermore, since the retrieval model in this study is focused on LC types, it is necessary to reclassify the original 17 LC types in the IGBP global vegetation classification scheme before matching the data. Based on the representative radiative characteristics of natural vegetation, the reliability of data quality, and the fact that the three-channel

algorithm was specifically optimized for vegetation/soil surfaces [33], this study retains only natural vegetation and bare soil-covered surfaces. The reclassified LC types are shown in Table II and Fig. 2. To ensure the purity of LC-type pixels, this study retains only those pixels where a single LC type constitutes 80% or more of the pixel.

### D. Overall Framework

In this study, two physically based methods for LST retrieval were employed, primarily establishing statistical relationships between CRE FY-3D PMW vertical polarization channel brightness temperatures and MODIS LST. The overall workflow of the process is shown in Fig. 3.

First, multiple variables from 2022 to 2023 were first extracted from multisource datasets and were subsequently preprocessed according to the spatial and temporal characteristics of the MYD11C1 LST data. For spatial collocation, the CRE FY-3D/MWRI brightness temperature, ERA5 variables, and DEM data were resampled to match the  $0.05^\circ$  spatial resolution of the MYD11C1 LST data. For temporal collocation, ERA5 variables with hourly temporal resolution were linearly interpolated to correspond to the FY-3D/MWRI observation times. MODIS TIR LST data were used as the ground truth for LST retrieval from PMW brightness temperature. The three-channel method requires the conversion of onboard brightness temperatures at 18.7, 36.5, and 89 GHz to surface brightness temperatures. The PWV-CLW method, on the other hand, uses onboard brightness temperatures from the 18.7- and 23.8-GHz channels, combined with PWV and CLW data, to establish the LST retrieval expression. Finally, a comparative analysis of the overall accuracy of the two

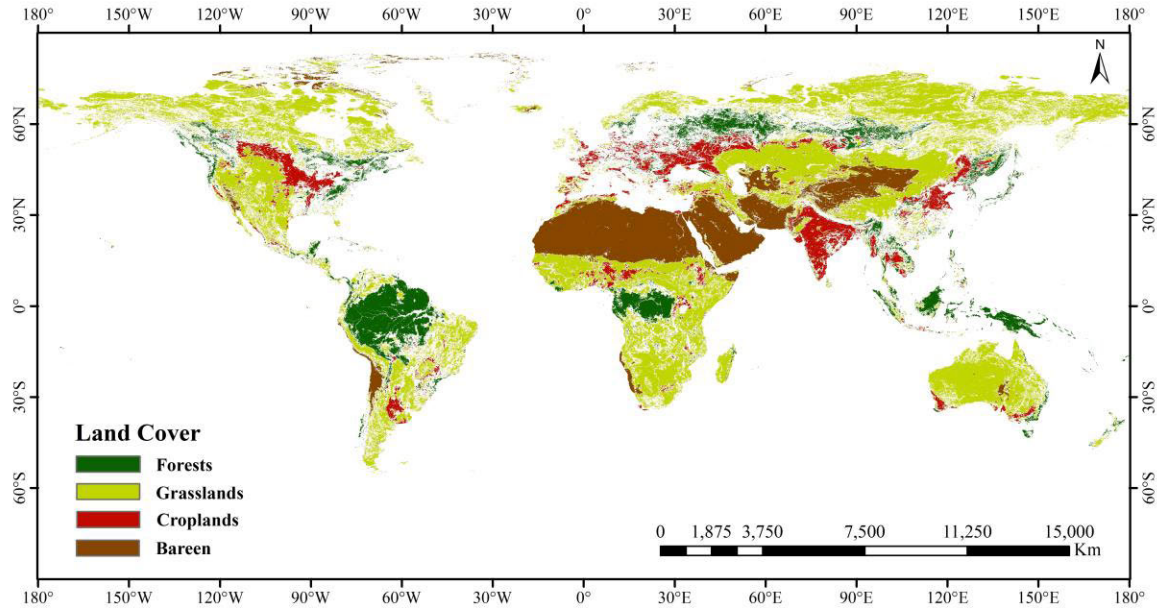


Fig. 2. Global LC map in 2022 after recategorization.

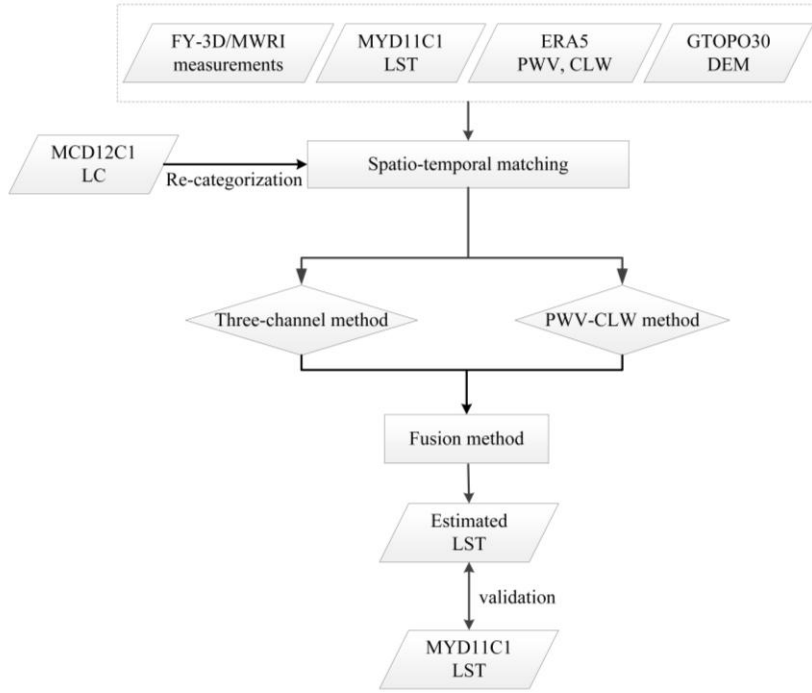


Fig. 3. Flowchart of the present study.

methods was conducted, along with an assessment of their performance across different LC types. This evaluation informed the development of a fusion method that integrates their respective strengths. The workflow of the study is illustrated in Fig. 3.

#### IV. RESULT

##### A. Coefficients of the Two LST Retrieval Methods

The coefficients were estimated using the least-squares method with data in 2022, and satellite measurements of

brightness temperature from both descending and ascending overpasses, MODIS LST products, and other datasets were employed to regressively fit the five coefficients in the two retrieval methods. The values of these coefficients are presented in Tables III and IV. The three-channel method is based on the relationship between surface emissivity at 18.7, 36.5, and 89.0 GHz and retrieves LST values from PMW data. The PWV-CLW method is derived from the microwave radiative transfer equation, incorporating PWV and CLW as supplementary inputs to parameterize the effect of clouds on

TABLE III  
COEFFICIENTS AND RMSE OF THE THREE-CHANNEL METHOD ALGORITHMS REGRESSED USING MODIS DATA

Coefficient	A	B	C	D	E	RMSE (K)
Ascending	0.9261	0.0635	0.9046	0.0483	42.4479	4.08
Descending	0.9010	-0.0154	1.3160	0.0667	36.9183	2.79

TABLE IV  
COEFFICIENTS AND RMSE OF THE PWV-CLW RETRIEVAL METHOD REGRESSED USING MODIS DATA

Coefficient	a <sub>1</sub>	a <sub>2</sub>	a <sub>3</sub>	a <sub>4</sub>	a <sub>5</sub>	RMSE (K)
Ascending	1.2973	1.1981	0.0153	5.1396	-46.4419	4.36
Descending	1.3609	2.2733	1.7027	3.3695	-40.0000	3.21

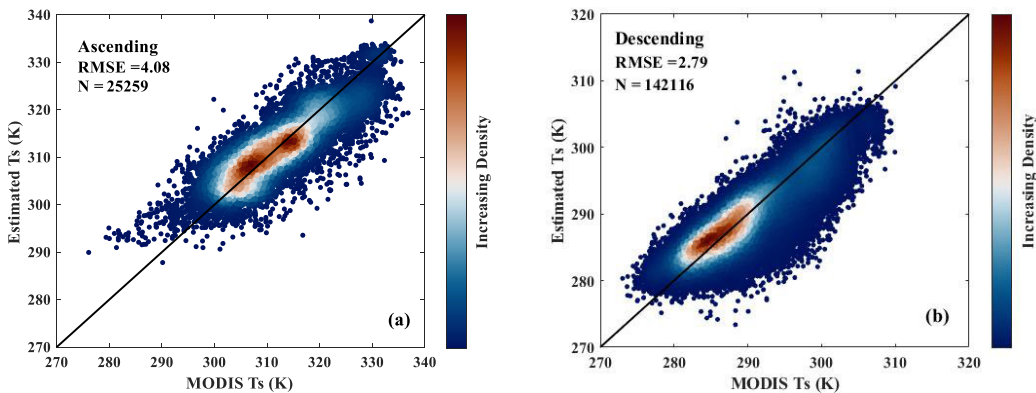


Fig. 4. Density scatterplots of three-channel method for calibration at (a) ascending overpass and (b) descending overpass.

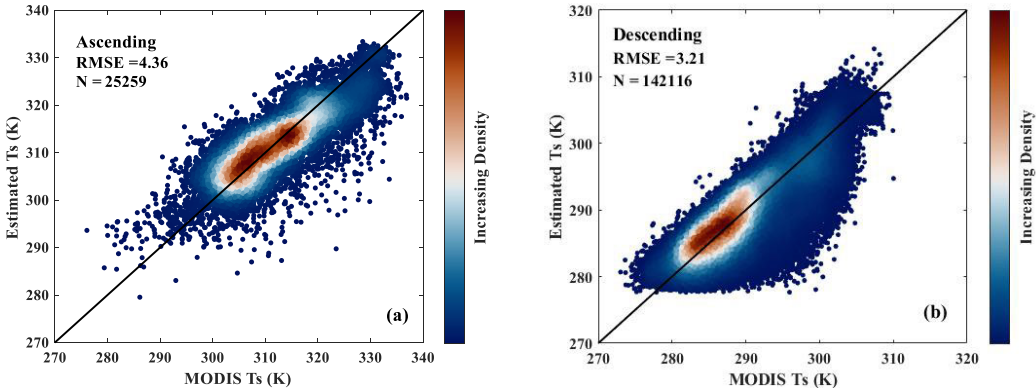


Fig. 5. Density scatterplots of PWV-CLW method for calibration at (a) ascending overpass and (b) descending overpass.

microwave radiation. These two methods feature coefficients with distinct physical meanings.

According to the results presented in Figs. 4 and 5, the root-mean-square error (RMSE) for the three-channel method was 4.08 and 2.79 K for ascending and descending overpasses, respectively. For the PWV-CLW method, the RMSE values were 4.36 and 3.21 K for ascending and descending overpasses, respectively. The superior accuracy of descending orbits compared to ascending orbits is attributed to their operational timing, with descending orbits acquiring data during nighttime periods, while ascending orbits operate during daylight hours. This temporal preference is justified by the substantial reduction in LST heterogeneity under nighttime conditions, where the absence of solar illumination minimizes thermal radiation interference and surface cooling

effects. The temporal variability of PWV and CLW in ERA5 reanalysis data may introduce interpolation errors during the temporal synchronization of MWRI and ERA5 datasets. This uncertainty is further compounded by the sensitivity of the MYD11C1 to PWV and CLW variations, as it is retrieved under clear-sky conditions. Such intrinsic limitations likely contribute to the diminished accuracy of the PWV-CLW algorithm. Therefore, the overall retrieval accuracy of the three-channel method is higher than that of the PWV-CLW method.

#### B. Validation Using MODIS LST Products

The MODIS LST product, with a spatial resolution of 0.05°, provides extensive spatial coverage and high accuracy, making

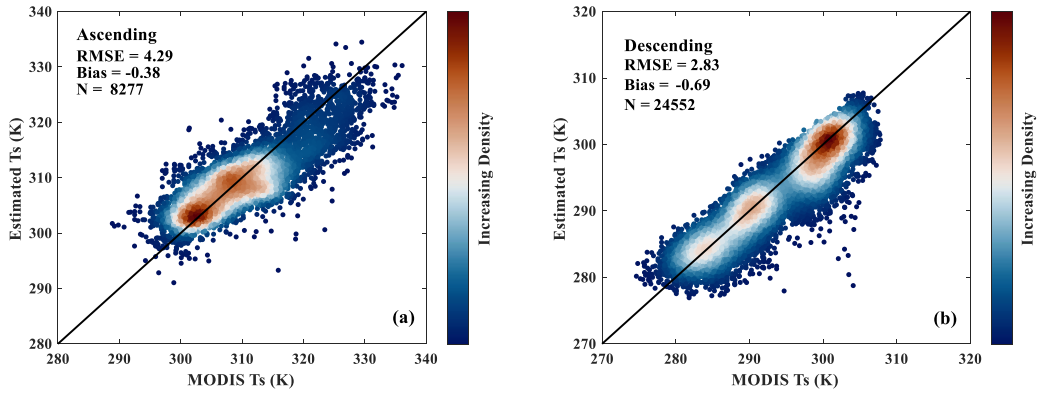


Fig. 6. Density scatterplots of three-channel method for validation at (a) ascending overpass and (b) descending overpass.

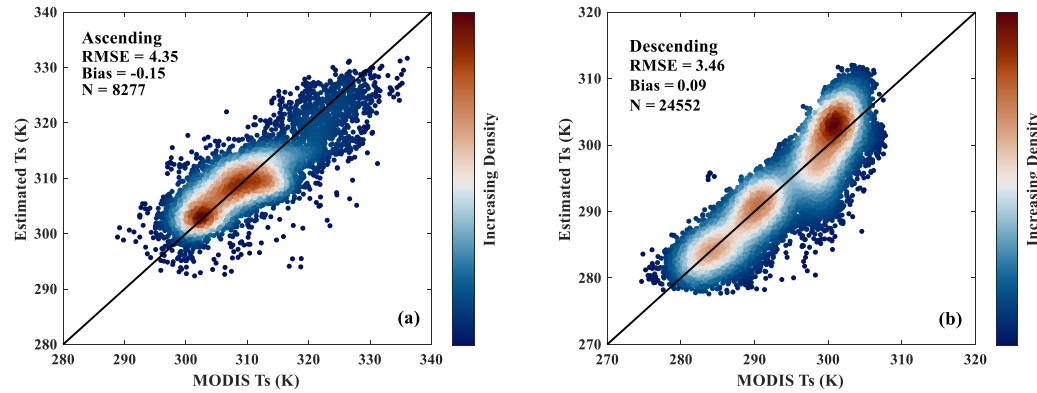


Fig. 7. Density scatterplots of PWV-CLW method for validation at (a) ascending overpass and (b) descending overpass.

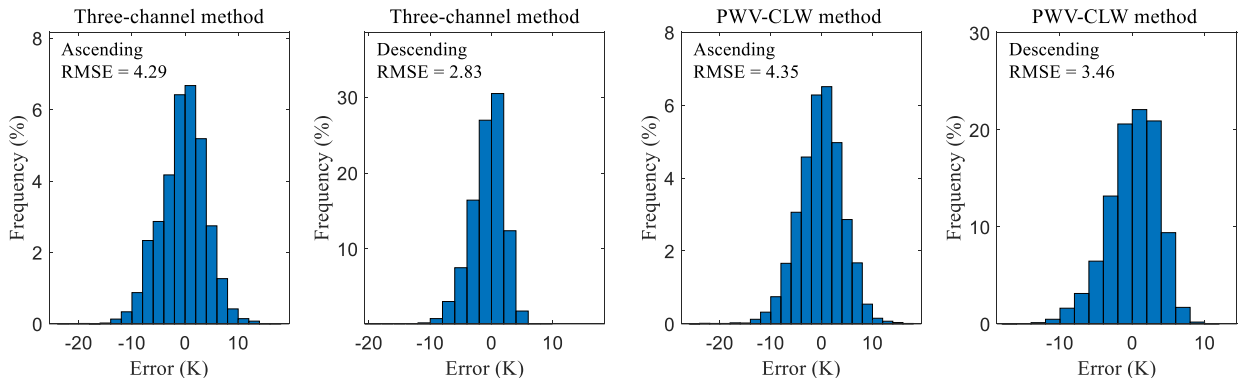


Fig. 8. Histogram of the difference between the actual LST and the estimated LST from the three-channel method and PWV-CLW method at ascending overpass and descending overpass, respectively.

it suitable for validating the FY-3D/MWRI LST estimates derived from CRE brightness temperatures in 2023.

Figs. 6 and 7 present the density scatter plots comparing LST retrievals using the two methods with MODIS-observed LST for ascending and descending overpasses, respectively. For the three-channel method, the RMSE and bias during ascending overpasses are 4.29 and  $-0.38$  K, respectively, while for descending overpasses, they are 2.83 and  $-0.69$  K, respectively. For the PWV-CLW method, the RMSE values are 4.35 and 3.46 K for ascending and descending overpasses, respectively, with corresponding bias values of  $-0.15$  and  $0.09$  K. Overall, the accuracy difference between the two methods is minimal. However, due to lower spatial heterogeneity

of LST at night, the accuracy of nighttime LST estimates is higher than that of the daytime estimates. Consistent with the training results, the three-channel method shows slightly better verification accuracy than the PWV-CLW method. Experimental results demonstrate that both methods produce reliable retrievals, confirming the effective application of CRE FY-3D/MWRI brightness temperatures for LST remote sensing retrieval. Fig. 8 illustrates the distribution of fitting errors. For the three-channel method, more than 75.4% of the daytime estimates and over 92.1% of the nighttime estimates fall within a  $\pm 5$  K range. Similarly, for the PWV-CLW method, 76.1% of the daytime estimates and 86.7% of the nighttime estimates are within this range. The three-channel method

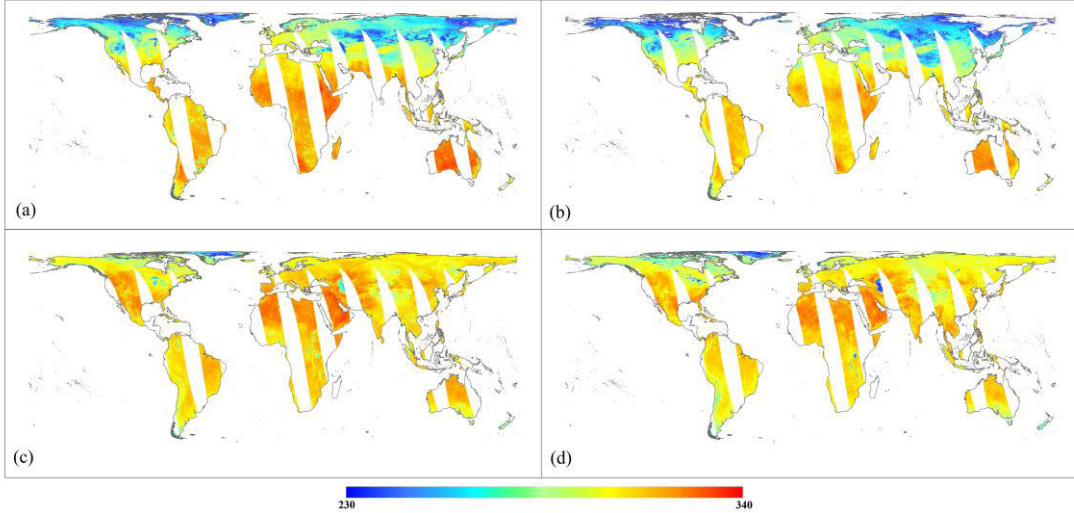


Fig. 9. Estimated ascending overpass FY-3D/MWRI LSTs of the global landmass on February 14 and August 14, 2023. February 14 and August 14 for (a) and (c) three-channel method and (b) and (d) PWV-CLW method. The unit for the LST is  $K$ .

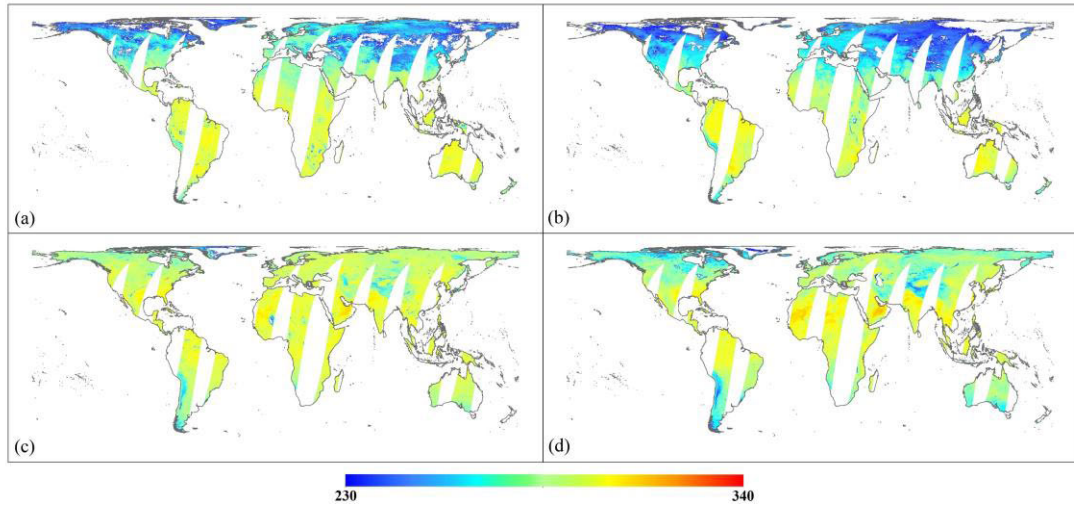


Fig. 10. Estimated descending overpass FY-3D/MWRI LSTs of the global landmass on February 14 and August 14, 2023. February 14 and August 14 for (a) and (c) three-channel method and (b) and (d) PWV-CLW method. The unit for the LST is  $K$ .

TABLE V  
COEFFICIENTS AND RMSE OF THE THREE-CHANNEL RETRIEVAL METHOD REGRESSED FOR DIFFERENT LC TYPES

Coefficient	A	B	C	D	E	RMSE (K)
1 - Forests	0.96 (0.91)	0.01 (0.34)	1.26 (1.22)	0.08 (0.10)	28.01 (38.47)	3.43 (3.66)
2 - Grasslands	0.94 (0.76)	-0.12 (0.10)	0.48 (0.83)	0.02 (0.07)	34.12 (74.28)	4.58 (2.40)
3 - Croplands	0.90 (0.67)	-0.29 (-0.15)	0.10 (0.66)	0.01 (0.06)	45.68 (97.61)	4.35 (2.67)
4 - Barren	0.92 (0.92)	0.13 (0.00)	1.17 (1.40)	0.06 (0.07)	46.81 (31.12)	3.90 (2.78)

and the PWV-CLW method, utilizing high spatial resolution FY-3D/MWRI brightness temperature data, were applied to produce an LST distribution map of the global landmass. Figs. 9 and 10 illustrate the estimated daytime and nighttime LSTs on February 14 and August 14, 2003, respectively. The results demonstrate that the estimated LST effectively captures temperature patterns across the global landmass.

## V. DISCUSSION

### A. Model Performance Over Different LC Types

In this study, LC types were reclassified into four categories: forest, grassland, cropland, and barren. To further evaluate

model performance, regression coefficients were fit separately for daytime and nighttime models across the different LC types, with corresponding biases and RMSEs calculated. The regression coefficients derived from training are presented in Tables V and VI. The number in brackets represents the coefficients and RMSE of the descending overpass. The validation results are shown in Fig. 11.

The performance of the method for each LC type was evaluated based on the reclassified LC types, and the accuracy of the two methods in ascending overpass and descending overpass was verified. The results are shown in Fig. 12.

TABLE VI  
COEFFICIENTS AND RMSE OF THE PWV-CLW RETRIEVAL METHOD REGRESSED FOR DIFFERENT LC TYPES

Coefficient	$a_1$	$a_2$	$a_3$	$a_4$	$a_5$	RMSE (K)
1 - Forests	2.57 (1.16)	0.65 (0.54)	1.64 (4.07)	2.51 (2.25)	-40.00 (-4.19)	3.37 (2.72)
2 - Grasslands	1.32 (1.66)	1.07 (2.42)	-0.88 (-3.76)	4.59 (2.81)	-40.00 (-40.00)	4.93 (2.57)
3 - Croplands	1.42 (1.85)	0.85 (1.99)	1.26 (-3.63)	3.80 (2.97)	-40.00 (-40.00)	5.04 (2.88)
4 - Barren	1.02 (1.35)	1.59 (2.28)	7.82 (2.42)	7.99 (3.49)	-40.00 (-40.00)	4.03 (3.23)

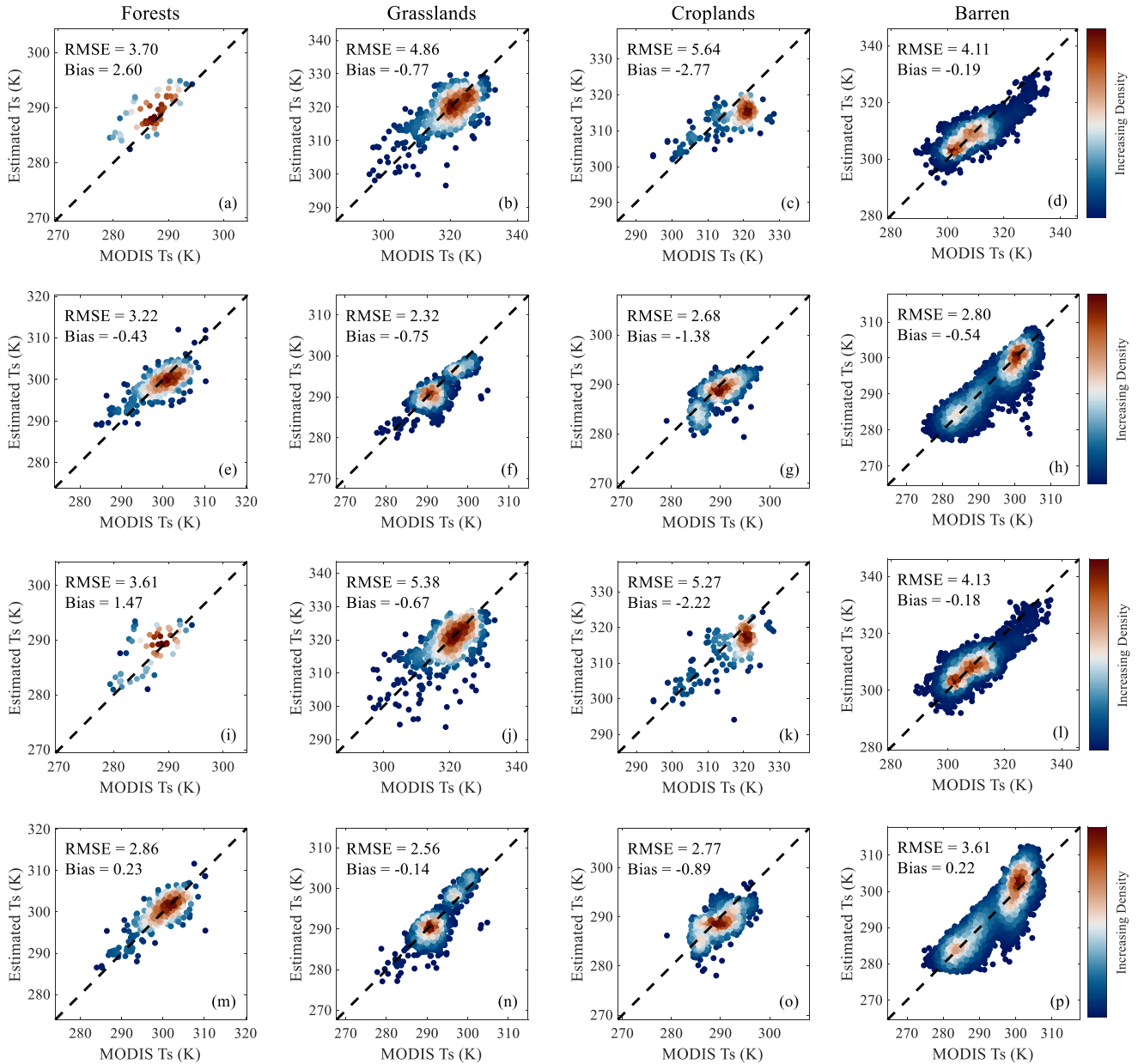


Fig. 11. Density scatterplots of estimated LST and MODIS LST for different LC types in ascending overpass and descending overpass. Comparative results of the three-channel method for (a)–(d) four surface cover types of forests, grasslands, croplands, and barren land in ascending overpass, respectively; and (e)–(h) descending overpass. Results of the PWV-CLW method for (i)–(l) four surface cover types in ascending overpass and (m)–(p) descending overpass.

After quality control, sample sizes for forest and cropland were relatively small, while barren areas exhibited the largest sample size. Specifically, the complex growth conditions in forested regions introduced greater instability, reducing data quality and leading to the exclusion of forest data during quality control. As a result, the limited sample size for forests

reduced its representativeness in the analysis. Fig. 11 demonstrates that both methods exhibit similar performance trends, as highlighted by the histogram in Fig. 12. During daytime (ascending overpass), the accuracy for grassland and cropland LC types is lower, with RMSE values ranging from 4 to 6 K for both methods. This lower accuracy can be attributed to the

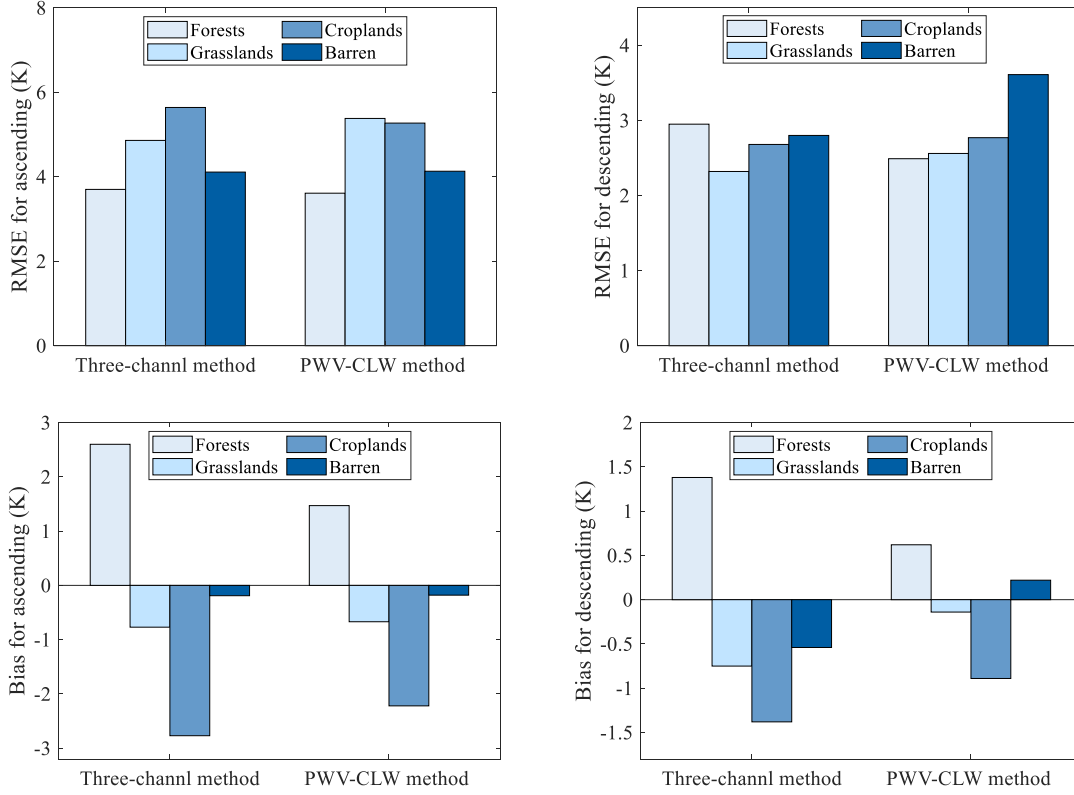


Fig. 12. RMSE and bias histograms of the three-channel method and the PWV-CLW method for different LC types in ascending overpass and descending overpass.

TABLE VII  
RMSE AND BIAS OF LST ESTIMATES BASED ON FY-3D/MWRI DATA

Method	Pass type	Forests	Grasslands	Croplands	Barren
Three-channel method	Ascending	3.70 (2.60)	4.86 (-0.77) *	5.64 (-2.77)	4.11 (-0.19) *
	Descending	3.22 (-0.43)	2.32 (-0.75) *	2.68 (-1.38) *	2.80 (-0.54) *
PWV-CLW method	Ascending	3.61 (1.47) *	5.38 (-0.67)	5.27 (-2.22) *	4.13 (-0.18)
	Descending	2.86 (0.23) *	2.56 (-0.14)	2.77 (-0.89)	3.61 (0.22)

significant variability in vegetation density and soil moisture in grasslands, coupled with intense solar radiation, which causes rapid increases in LST. These factors destabilize microwave radiation and complicate the retrieval process. In contrast, barren areas, characterized by simpler surface features and minimal external influences, maintain relatively uniform temperatures, leading to higher retrieval accuracy. At nighttime (descending overpass), retrieval accuracy for grassland LC types improves, with both methods achieving RMSE values around 2 K and showing smaller biases. This improvement may result from higher moisture content in grasslands at night, which stabilizes heat retention and enhances retrieval accuracy. Conversely, agricultural areas exhibit greater temperature variability due to fluctuating soil moisture and crop growth, which adversely affect retrieval accuracy.

The validation accuracy and bias of the two methods across different LC types are summarized in Table VII. The values in parentheses represent the bias, and the column marked with an asterisk (\*) indicates that the inversion method corresponding to this symbol provides superior accuracy for the respective

vegetation cover type. The results reveal the following key observations for various LC types. During the daytime, the PWV-CLW method demonstrates better accuracy for forests and croplands, while the three-channel method shows higher accuracy for grasslands and barren areas. At nighttime, the PWV-CLW method remains more accurate for forests, while the three-channel method outperforms for grasslands, croplands, and barren areas.

#### B. Method Fusion

In this study, we investigated the three-channel method and PWV-CLW method for estimating LST across different LC types. The results reveal that the performance of the two methods varies depending on the LC type. Specifically, during daytime, the PWV-CLW method demonstrated higher accuracy for forests and croplands, whereas the three-channel method performed better for grasslands and barren lands. At nighttime, the PWV-CLW method proved more effective for forests, while the three-channel method yielded more accurate results for grasslands, croplands, and barren lands. To optimize the

TABLE VIII  
LST RETRIEVAL METHOD SELECTION GUIDE FOR ASCENDING AND DESCENDING OVERPASS UNDER DIFFERENT LC TYPES

Method	Ascending				Descending			
	1	2	3	4	1	2	3	4
Three-channel method		✓		✓		✓	✓	✓
PWV-CLW method	✓		✓		✓			

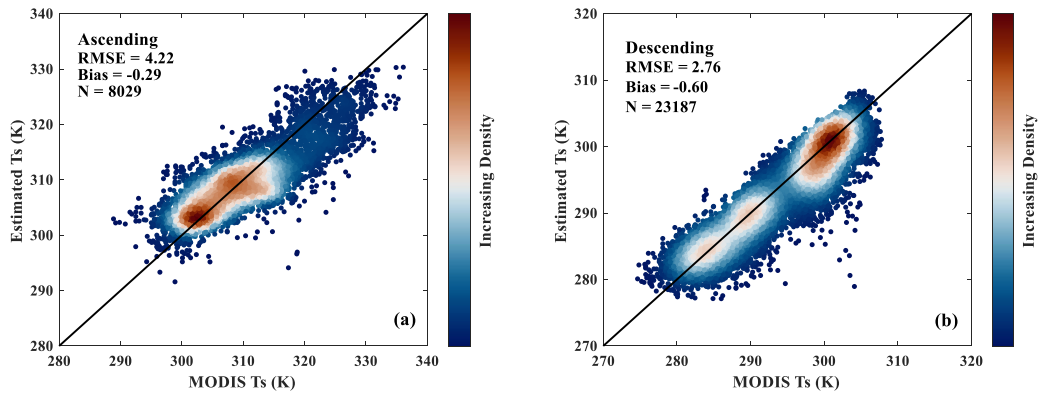


Fig. 13. Density scatterplots of LSTs using fusion method at (a) ascending overpass and (b) descending overpass.

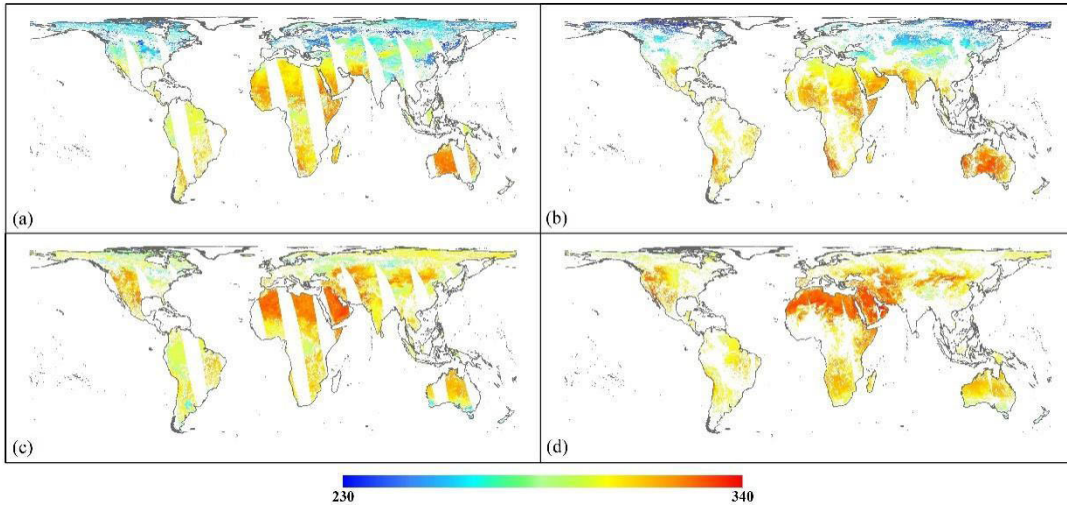


Fig. 14. Ascending overpass LST distribution for February 14 and August 14, 2023, estimated using the fusion method from (left) FY-3D/MWRI LST and (right) MODIS LST product based on recategorization LC types. (a) February 14, fusion method; (b) February 14, MODIS LST; (c) August 14, fusion method; and (d) August 14, MODIS LST.

overall accuracy of LST estimation, it is crucial to select the most precise method for each LC type. To address the limitations of individual retrieval methods, we propose a fusion method that capitalizes on their respective strengths while mitigating their weaknesses. This method identifies the most accurate retrieval approach for each specific LC type and integrates them into a unified framework. By doing so, it maximizes the strengths of both methods and minimizes the uncertainties in the inversion results, ensuring a more robust and reliable estimation of LST. Table VIII illustrates the fusion of four LC types; numbers 1, 2, 3, and 4 represent forest, grassland, cropland, and barren, respectively. The most accurate retrieval method is selected from the two inversion approaches for each type, based on ascending and descending

overpasses. The combined model's inversion results are subsequently validated against MODIS LST data to evaluate its performance enhancements.

Fig. 13 illustrates the density scatterplots of LSTs derived using the fusion method for both ascending (a) and descending (b) overpasses. The scatterplots indicate a high correlation between the fused LST results (combining the three-channel and PWV-CLW methods) and the MODIS LST product. The RMSE and bias for the ascending overpass are 4.22 and  $-0.29$  K, respectively, while for the descending overpass, they are 2.76 and  $-0.6$  K, respectively. Compared to the individual methods, the fusion approach effectively reduces errors across different LC types and improves retrieval accuracy.

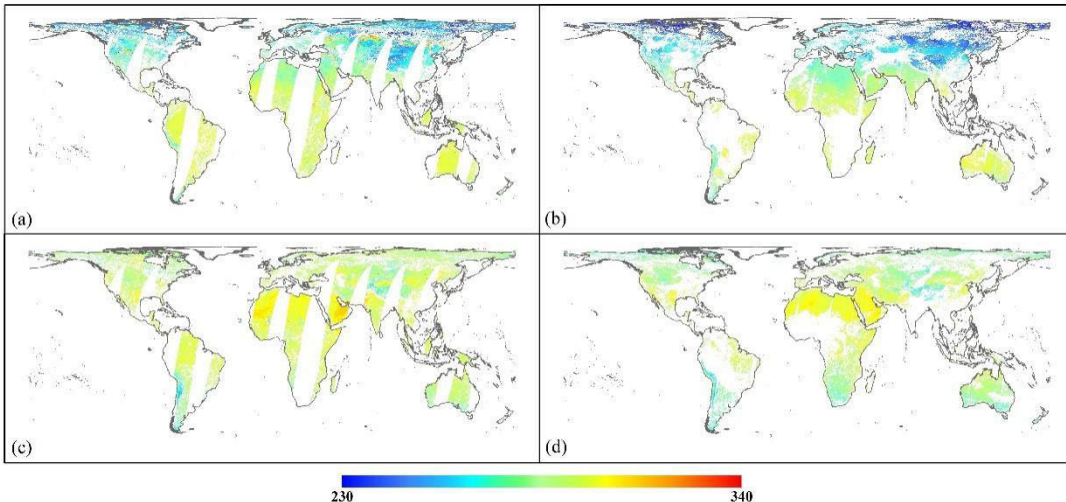


Fig. 15. Descending overpass LST distribution for February 14 and August 14, 2023, estimated using the fusion method from (left) FY-3D/MWRI LST and (right) MODIS LST product based on recategorization LC types. (a) February 14, fusion method; (b) February 14, MODIS LST; (c) August 14, fusion method; and (d) August 14, MODIS LST.

Figs. 14 and 15 provide insights into seasonal variations and the impact of LC reclassification on LST estimates. A comparison between the fused LST and the MODIS LST product shows that the fusion method produces estimates closer to the observed values. By leveraging the enhanced spatial resolution of FY-3D/MWRI LST data, the fusion approach better captures temperature variations, particularly in regions characterized by diverse LC types and significant meteorological changes. Consequently, the fusion method consistently delivers accurate and reliable LST estimates for both ascending and descending overpasses. By integrating the strengths of the three-channel and PWV-CLW methods based on LC-specific accuracy, this fusion approach significantly enhances LST retrieval. The LC-specific selection of methods enables a tailored and efficient utilization of available techniques, ultimately yielding more precise and comprehensive LST estimates. It is noteworthy that the proposed fusion method reveals no significant increase in model complexity, regarding either data sources or calculation process. This study underscores the importance of method fusion for achieving robust and reliable LST results, especially in regions with heterogeneous LC and dynamic meteorological conditions.

## VI. CONCLUSION

In this study, we enhanced the grid resolution to one-fourth of the original spatial sampling frequency, using FY-3D/MWRI multichannel brightness temperatures at a spatial resolution of 6.25 km as the primary input data. We applied two PMW LST retrieval methods: the three-channel method and PWV-CLW method. The retrieval accuracy under different LC types was also discussed. A fusion method was proposed based on the strengths and weaknesses of the two methods for different LC types, followed by comprehensive validation and analysis.

We trained both methods using FY-3D/MWRI images covering various periods throughout 2022 and the MYD11C1 LST product. Validation was conducted with global MYD11C1

data from selected periods in 2023. The three-channel method demonstrated higher accuracy compared to the PWV-CLW method, albeit with a slightly larger bias. The accuracy for ascending and descending overpasses was 4.29 and 2.83 K, respectively, with biases of  $-0.38$  and  $-0.69$  K. The PWV-CLW method achieved accuracies of 4.35 and 3.46 K, with biases of  $-0.15$  and  $0.09$  K. Both methods exhibit higher accuracy at night compared to daytime. The retrieval results indicate that the use of CRE FY-3D/MWRI brightness temperature data ensures strong spatial representativeness and reliable performance across both methods.

Using high spatial resolution data, a comprehensive evaluation of stability and accuracy was conducted for two methods across various LC types. The findings reveal that the three-channel method exhibits superior performance for estimating surface temperature in grasslands and bare land during the day, as well as for grasslands, croplands, and bare land at night, achieving RMSE values ranging from 2.3 to 2.8 K. Conversely, the PWV-CLW method demonstrates higher accuracy for surface temperature estimation in forests and croplands during the day and outperforms in forested areas at night. Based on these findings, we propose a fusion method designed to optimize surface temperature retrieval for specific LC types. The fusion method achieved accuracies of 4.22 and 2.76 K for ascending and descending overpasses, with biases of  $-0.29$  and  $-0.6$  K, respectively. The fusion method demonstrated a significant improvement in overall inversion accuracy compared to the individual methods. By integrating the strengths of multiple models, the combined inversion approach delivers more robust and reliable results, particularly under complex surface conditions or when substantial data noise is present.

This research offers several key improvements over previous studies. First, unlike earlier studies that often used relatively coarse 25-km spatial resolution data for PMW LST retrieval, this study utilizes high spatial resolution data, resulting in superior spatial accuracy, more precise temperature

estimates, and enhanced adaptability. Second, by integrating LC information, this study analyzes the microwave radiation characteristics of different LC types under varying meteorological conditions. The fusion of the two methods led to higher overall retrieval accuracy, bringing the LST estimates closer to MODIS-derived LST values. This fusion approach not only improves retrieval accuracy but also enables the generation of all-weather LST estimates, which is crucial for continuous monitoring of the Earth's surface temperature. However, the proposed method is not without limitations. While resampling and interpolation techniques were employed to harmonize scale differences between various input variables and the target LST, these processes inevitably introduce some degree of error. Furthermore, the study was constrained by limited access to high spatial resolution data and in situ measurements, which precluded validation against site-specific measured data under clear-sky conditions. Future research should prioritize the collection of more extensive in situ measurements and facilitate comprehensive validation. Additionally, expanding the application of high-resolution PMW brightness temperature data to a wider range of scenarios could unlock new opportunities and provide deeper insights into PMW remote sensing retrieval methodologies.

In conclusion, this study demonstrates that the use of FY-3D/MWRI brightness temperature data at a spatial resolution of 6.25 km is effective for LST retrieval, yielding satisfactory accuracy. Additionally, we proposed an LC-type-specific fusion method combining two inversion approaches, which significantly improves the overall retrieval precision. This fusion method enhances LST estimation by effectively addressing the spatial heterogeneity and atmospheric effects, making it more robust across diverse LC types. Furthermore, the fusion of both methods enables all-weather LST retrieval, offering a reliable and continuous data source that can be applied under various environmental and climatic conditions. The results highlight the potential of high spatial resolution PMW data for operational LST monitoring, providing a valuable tool for future remote sensing applications.

## REFERENCES

- [1] Z. Li et al., "Satellite remote sensing of global Land Surface Temperature: Definition, methods, products, and applications," *Rev. Geophys.*, vol. 61, no. 1, Mar. 2023, Art. no. e2022RG000777.
- [2] S.-B. Duan, Z.-L. Li, B.-H. Tang, H. Wu, and R. Tang, "Generation of a time-consistent land surface temperature product from MODIS data," *Remote Sens. Environ.*, vol. 140, pp. 339–349, Jan. 2014.
- [3] Z. Wan and Z.-L. Li, "A physics-based algorithm for retrieving land-surface emissivity and temperature from EOS/MODIS data," *IEEE Trans. Geosci. Remote Sens.*, vol. 35, no. 4, pp. 980–996, Jul. 1997.
- [4] M. Anderson, J. Norman, W. Kustas, R. Houborg, P. Starks, and N. Agam, "A thermal-based remote sensing technique for routine mapping of land-surface carbon, water and energy fluxes from field to regional scales," *Remote Sens. Environ.*, vol. 112, no. 12, pp. 4227–4241, Dec. 2008.
- [5] Z.-L. Li et al., "Satellite-derived Land Surface Temperature: Current status and perspectives," *Remote Sens. Environ.*, vol. 131, pp. 14–37, Apr. 2013.
- [6] M. Auger, R. Morrow, E. Kestenare, J.-B. Sallée, and R. Cowley, "Southern ocean in-situ temperature trends over 25 years emerge from interannual variability," *Nature Commun.*, vol. 12, no. 1, Jan. 2021, Art. no. 514.
- [7] S.-B. Duan et al., "Improving monthly mean Land Surface Temperature estimation by merging four products using the generalized three-cornered hat method and maximum likelihood estimation," *Remote Sens. Environ.*, vol. 302, Mar. 2024, Art. no. 113989.
- [8] C. Ru, S.-B. Duan, X.-G. Jiang, Z.-L. Li, C. Huang, and M. Liu, "An extended SW-TES algorithm for Land Surface Temperature and emissivity retrieval from ECOSTRESS thermal infrared data over urban areas," *Remote Sens. Environ.*, vol. 290, May 2023, Art. no. 113544.
- [9] J. C. Jiménez-Muñoz and J. A. Sobrino, "A generalized single-channel method for retrieving Land Surface Temperature from remote sensing data," *J. Geophys. Research: Atmos.*, vol. 108, no. D22, Nov. 2003, Art. no. 4688.
- [10] J. Cristóbal, J. Jiménez-Muñoz, A. Prakash, C. Mattar, D. Skoković, and J. Sobrino, "An improved single-channel method to retrieve Land Surface Temperature from the Landsat-8 thermal band," *Remote Sens.*, vol. 10, no. 3, p. 431, Mar. 2018.
- [11] J. C. Price, "Estimating surface temperatures from satellite thermal infrared data—A simple formulation for the atmospheric effect," *Remote Sens. Environ.*, vol. 13, no. 4, pp. 353–361, Sep. 1983.
- [12] F. Becker and Z.-L. Li, "Towards a local split window method over land surfaces," *Int. J. Remote Sens.*, vol. 11, no. 3, pp. 369–393, Mar. 1990.
- [13] Z. Wan and J. Dozier, "A generalized split-window algorithm for retrieving land-surface temperature from space," *IEEE Trans. Geosci. Remote Sens.*, vol. 34, no. 4, pp. 892–905, Jul. 1996.
- [14] J. Zhao, B.-H. Tang, and O. Sima, "A nonlinear split-window algorithm for retrieving land surface temperatures from fengyun-4B thermal infrared data," *IEEE Trans. Geosci. Remote Sens.*, vol. 62, 2024, Art. no. 5000612.
- [15] A. R. Gillespie et al., "Temperature and emissivity separation from advanced spaceborne thermal emission and reflection radiometer (ASTER) images," *Proc. SPIE*, vol. 2817, pp. 82–94, Oct. 1996.
- [16] S. Zhou and J. Cheng, "An improved temperature and emissivity separation algorithm for the advanced Himawari imager," *IEEE Trans. Geosci. Remote Sens.*, vol. 58, no. 10, pp. 7105–7124, Oct. 2020.
- [17] S.-B. Duan, Z.-L. Li, and P. Leng, "A framework for the retrieval of all-weather land surface temperature at a high spatial resolution from polar-orbiting thermal infrared and passive microwave data," *Remote Sens. Environ.*, vol. 195, pp. 107–117, Jun. 2017.
- [18] S.-B. Duan et al., "Land Surface Temperature retrieval from passive microwave satellite observations: State-of-the-Art and future directions," *Remote Sens.*, vol. 12, no. 16, p. 2573, Aug. 2020.
- [19] P. Wu et al., "A two-step deep learning framework for mapping gapless all-weather Land Surface Temperature using thermal infrared and passive microwave data," *Remote Sens. Environ.*, vol. 277, Aug. 2022, Art. no. 113070.
- [20] M. J. McFarland, R. L. Miller, and C. M. U. Neale, "Land Surface Temperature derived from the SSM/I passive microwave brightness temperatures," *IEEE Trans. Geosci. Remote Sens.*, vol. 28, no. 5, pp. 839–845, Sep. 1990.
- [21] J. T. Pulliainen, J. Grandell, and M. T. Hallikainen, "Retrieval of surface temperature in boreal forest zone from SSM/I data," *IEEE Trans. Geosci. Remote Sens.*, vol. 35, no. 5, pp. 1188–1200, Sep. 1997.
- [22] M. Owe and A. A. Van De Griend, "On the relationship between thermodynamic surface temperature and high-frequency (37 GHz) vertically polarized brightness temperature under semi-arid conditions," *Int. J. Remote Sens.*, vol. 22, no. 17, pp. 3521–3532, Jan. 2001.
- [23] T. R. H. Holmes, R. A. M. De Jeu, M. Owe, and A. J. Dolman, "Land Surface Temperature from Ka band (37 GHz) passive microwave observations," *J. Geophys. Research: Atmos.*, vol. 114, no. D4, Feb. 2009, Art. no. D04113.
- [24] J. Zhou, F. Dai, X. Zhang, S. Zhao, and M. Li, "Developing a temporally land cover-based look-up table (TL-LUT) method for estimating land surface temperature based on AMSR-E data over the Chinese landmass," *Int. J. Appl. Earth Observ. Geoinf.*, vol. 34, pp. 35–50, Feb. 2015.
- [25] F.-C. Zhou, Z.-L. Li, H. Wu et al., "A practical two-stage algorithm for retrieving Land Surface Temperature from AMSR-E data—a case study over China," *IEEE J. Sel. Topics Appl. Earth Observ. Remote Sens.*, vol. 11, no. 6, pp. 1939–1948, Jun. 2018.
- [26] E. G. Njoku and L. Li, "Retrieval of land surface parameters using passive microwave measurements at 6–18 GHz," *IEEE Trans. Geosci. Remote Sens.*, vol. 37, no. 1, pp. 79–93, Jan. 1999.
- [27] F. Aires, C. Prigent, W. B. Rossow, and M. Rothstein, "A new neural network approach including first guess for retrieval of atmospheric water vapor, cloud liquid water path, surface temperature, and emissivities over land from satellite microwave observations," *J. Geophys. Res., Atmos.*, vol. 106, no. 14, pp. 14887–14907, Jul. 2001.

- [28] W. Tan, C. Wei, Y. Lu, and D. Xue, "Reconstruction of all-weather daytime and nighttime MODIS Aqua-Terra Land Surface Temperature products using an XGBoost approach," *Remote Sens.*, vol. 13, no. 22, p. 4723, Nov. 2021.
- [29] Y. Zhong, L. Meng, Z. Wei, J. Yang, W. Song, and M. Basir, "Retrieval of all-weather 1 km Land Surface Temperature from combined MODIS and AMSR2 data over the Tibetan Plateau," *Remote Sens.*, vol. 13, no. 22, p. 4574, Nov. 2021.
- [30] Y. Lian, S.-B. Duan, C. Huang, W. Han, and M. Liu, "Generation of spatial-seamless AMSR2 Land Surface Temperature in China during 2012–2020 using a deep neural network," *IEEE Trans. Geosci. Remote Sens.*, vol. 61, 2023, Art. no. 5300618.
- [31] K. Mao et al., "A general paradigm for retrieving soil moisture and surface temperature from passive microwave remote sensing data based on artificial intelligence," *Remote Sens.*, vol. 15, no. 7, p. 1793, Mar. 2023.
- [32] A. Basist, N. C. Grody, T. C. Peterson, and C. N. Williams, "Using the special sensor microwave/imager to monitor land surface temperatures, wetness, and snow cover," *J. Appl. Meteorol.*, vol. 37, no. 9, pp. 888–911, Sep. 1998.
- [33] X. J. Han, S. B. Duan, C. Huang, and Z. L. Li, "Cloudy land surface temperature retrieval from three-channel microwave data," *Int. J. Remote Sens.*, vol. 40, nos. 5–6, pp. 1793–1807, Mar. 2019.
- [34] F. Weng and N. C. Grody, "Physical retrieval of land surface temperature using the special sensor microwave imager," *J. Geophys. Res., Atmos.*, vol. 103, no. 8, pp. 8839–8848, Apr. 1998.
- [35] C. Huang et al., "A physically based algorithm for retrieving Land Surface Temperature under cloudy conditions from AMSR2 passive microwave measurements," *Int. J. Remote Sens.*, vol. 40, nos. 5–6, pp. 1828–1843, Mar. 2019.
- [36] C. Huang, S. Zhang, W. Han, X. Feng, and S.-B. Duan, "Retrieval of cloudy Land Surface Temperature from AMSR2 brightness temperature, precipitable water vapour and cloud liquid water," *Int. J. Remote Sens.*, vol. 45, nos. 19–20, pp. 7518–7534, Oct. 2024.
- [37] A. Guha and V. Lakshmi, "Use of the scanning multichannel microwave radiometer (SMMR) to retrieve soil moisture and surface temperature over the central United States," *IEEE Trans. Geosci. Remote Sens.*, vol. 42, no. 7, pp. 1482–1494, Jul. 2004.
- [38] L. Meng, Y. He, J. Chen, and Y. Wu, "Neural network retrieval of ocean surface parameters from SSM/I data," *Monthly Weather Rev.*, vol. 135, no. 2, pp. 586–597, Feb. 2007.
- [39] X. Huang et al., "Seamless reconstruction of AMSR-E Land Surface Temperature swath gaps for China's landmass," *IEEE Trans. Geosci. Remote Sens.*, vol. 61, 2023, Art. no. 4411615.
- [40] T. Hihara, M. Kubota, and A. Okuro, "Evaluation of sea surface temperature and wind speed observed by GCOM-W1/AMSR2 using in situ data and global products," *Remote Sens. Environ.*, vol. 164, pp. 170–178, Jul. 2015.
- [41] F. Zhou, X. Han, S. Tang, G. Cao, X. Song, and B. Wang, "A physics-based method for retrieving land surface emissivities from FengYun-3D microwave radiation imager data," *Remote Sens.*, vol. 16, no. 2, p. 352, Jan. 2024.
- [42] G. Cao, F. Zhou, and Z. Zheng, "Improvement method of Land Surface Temperature remotely sensed by geostationary and polar orbiting meteorological satellites," *Meteorolog. Monthly*, vol. 49, no. 3, pp. 318–326, 2023.
- [43] L. Dong, S. Tang, F. Wang, M. Cosh, X. Li, and M. Min, "Inversion and validation of FY-4A official Land Surface Temperature product," *Remote Sens.*, vol. 15, no. 9, p. 2437, May 2023.
- [44] Y. Zhu, M. Wu, and Y. Bao, "LST reversion and downscaling based on FY -3D/ MWRI L1B brightness temperature data," *Remote Sens. Natural Resour.*, vol. 33, no. 3, pp. 27–35, 2021.
- [45] B. Wang, P. Guo, and C. Meng, "Retrieval and verification of land surface temperature in China based on an FY-3Dmicrowave radiation imager," *Trans. Atmos. Sci.*, vol. 45, no. 1, pp. 112–123, 2022.
- [46] Y. Bai, Z. Zheng, J. Shen, N. Xu, G. Cao, and H. Xiao, "Spatial resolution enhancement of microwave radiation imager (MWRI) data," *Remote Sens.*, vol. 17, no. 6, p. 1034, Mar. 2025.